

# Aerodynamic and Static Coupling Simulations of the Pazy Wing with Transitional CFD for the Third Aeroelastic Prediction Workshop

Markus Ritter\* and Michael Fehrs†

*DLR - Institute of Aeroelasticity, Bunsenstr  e 10, 37073 G  ttingen, Germany*

Christoph Mertens‡

*Faculty of Aerospace Engineering, Delft University of Technology, 2629 HS Delft, The Netherlands*

**The *Pazy Wing* test case is a benchmark for the investigation of aeroelastic effects at very large deflections. Tip deformations in the order of 50% span were measured in wind tunnel tests which renders this model highly attractive for the validation of numerical aeroelastic methods and tools for geometrically nonlinear, large deflection analyses. The present work is focused on high fidelity aerodynamic and aeroelastic simulations of the wing using RANS and URANS with transition modeling in order to capture nonlinear effects originating from the shape of the wing and the low Reynolds number. Steady and unsteady aerodynamic as well as static coupling simulations with a nonlinear structural model are presented, the impact of the different transition and turbulence modeling techniques is depicted. This work supports the *Large Deflection Working Group (LDWG)*, which is one of the sub-groups of the 3<sup>rd</sup> *Aeroelastic Prediction Workshop (AePW3)*.**

## I. Motivation and Introduction

**V**ERIFICATION and Validation of aeroelastic solvers are indispensable and require suitable data from other numerical methods or, preferably, from experiments. Unfortunately, comprehensive and publicly available experimental data sets of highly flexible test cases are scarce but such investigations are the topic of current research. The Pazy Wing was specifically designed to provide experimental data of a highly flexible aeroelastic test case which can be used for the validation of numerical methods in the nonlinear regime with large deflections. Particular features make this test case interesting for a broad audience. The geometry and the test conditions of the model are simple: A wing with rectangular planform, no taper, no sweep, and a symmetrical airfoil that operates in an incompressible flow regime (the Mach number is approximately 0.15 for the highest onflow velocity in the wind tunnel tests). These features allow for the application of a range of potential aerodynamic methods. However, difficulties arise with the Pazy Wing due to the low Reynolds numbers (approximately  $4.5 \cdot 10^5$  for the highest onflow velocity) and the large airfoil thickness which manifest in aerodynamic nonlinearities. Mainly laminar separation bubbles and early flow separation lead to strong dependencies of the aerodynamic loads on the angle of attack of the wing as will be discussed in the following.

The Pazy Wing wind tunnel models from Technion and TU Delft – the model investigated in this work – are shown in Fig. 1, the main dimensions are listed in Table 1.

Aeroelastic simulations (static coupling and flutter) that have been presented in the LDWG to analyze the behavior of the Pazy Wing are based on geometrically nonlinear structural methods – which are indispensable for this test case – and linear (potential) aerodynamics, mostly the UVLM and the DLM are applied. This combination offers advantages such as low computational cost, and even aerodynamic nonlinearities – due to stall, for instance – can be modeled by simple approaches [2–4]. These methods enable the evaluation of the stability boundary of the Pazy Wing which strongly depends on the combination of airspeed and static angle of attack due to the large structural deflections and the corresponding changes in the eigenvalues and mode shapes of the wing. The dynamic aeroelastic stability regions are illustrated in Fig. 2, for a range of onflow velocities (from 30 m/s to 110 m/s) and a range of angles of attack (from zero degrees to five degrees) [5].

---

\*Group leader in Loads Analysis and Aeroelastic Design department, Markus.Ritter@dlr.de

†Research Assistant, Michael.Fehrs@dlr.de

‡PhD Student, C.Mertens@tudelft.nl

**Table 1 Dimensions of the Pazy Wing Wind tunnel model.**

Property	Unit	Pazy Wing
Span	m	0.56
Chord (without tip rod)	m	0.1
Clamping section height	m	0.021
Clamping section diameter	m	0.12
Tip rod length	m	0.3
Tip rod diameter	m	0.01
Airfoil	-	NACA 0018



**Fig. 1 Pazy Wing in wind tunnel at Technion (left) [1]. Outer surface of the Pazy Wing from TU Delft in undeflected jig-shape with close up highlighting the sagging skin (foil cover) between the ribs.**

A new field, which is explored by current simulations, is limit cycle oscillations (LCO), which have been observed in several wind tunnel tests. LCOs are an inherently nonlinear phenomenon, and, relating to the Pazy Wing test case, are primarily induced by particular steady and unsteady viscous effects such as laminar separation bubbles, transition mechanisms, and (dynamic) stall. Furthermore, these nonlinearities strongly depend on the local shape of the wing's covering (a plastic thermal shrink film) which changes based on the instantaneous flow and structural conditions. Even at the unloaded state, the outer shape of the wing is complex due to the sagging of the foil covering between the ribs which yields a different airfoil section with reduced thickness and kinks. To investigate the aerodynamic effects resulting from these specifics and to address them in future aeroelastic simulations of the Pazy Wing, the potential aerodynamic methods, which have been used by the authors to date, are replaced by CFD-based aerodynamics that solve the RANS and URANS equations with proper methods for the modeling of transition and turbulence.

The objective of this work is thus the investigation of the steady aerodynamic characteristics of the rigid and deformed Pazy Wing based on CFD computations for fully turbulent and transitional boundary layer flows. To account for the true geometry of the wing – including local kinks and the sagging of the foil covering – a scan of the outer geometry of the TU Delft Pazy Wing was used as basis for the CFD grid generation. The insights acquired yield a better understanding of the flow physics of built up (rib) wings with complex outer shapes at low Reynolds numbers.

This work is a further contribution to the current activities of the *Large Deflection Working Group (LDWG)*, which is one of the sub-groups of the 3<sup>rd</sup> *Aeroelastic Prediction Workshop (AePW3)*<sup>1</sup>. The goal of the group's activities is

<sup>1</sup><https://nescacademy.nasa.gov/workshops/AePW3/public>

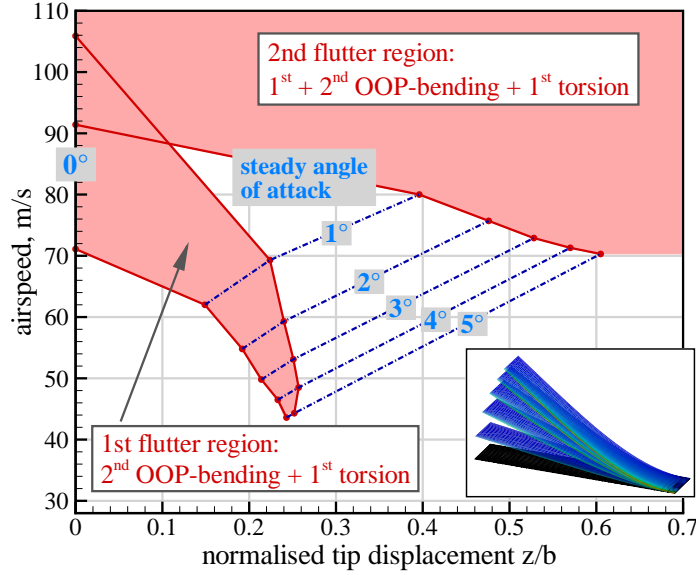


**Fig. 2** The dynamic aeroelastic stability regions of the Pazy Wing (as predicted by linearized models) show a strong dependence on the static structural deformation [5].

to investigate and model the aeroelastic behavior of the Pazy Wing test case [1, 3, 5–10]. All information required to setup and model the test case are publicly available, including detailed finite element (FE) models of the wing. Detailed information about the Pazy Wing and the LDWG are given in recent publications [1, 5–9].

## II. TU Delft Pazy Wing Wind Tunnel Experiment: Infrared Thermography Measurements

A wind tunnel experiment is conducted to support the CFD simulation results with validation data for the complex behavior of the boundary layer on the Pazy wing. The experiment is performed at the Open Jet Facility at Delft University of Technology, which has a freestream turbulence intensity of around  $Tu = 0.5\%$ . The test object is the TU Delft Pazy Wing that was previously scanned with the 3D scanner to provide the reference shape for the CFD simulations as mentioned above. For the experiment, the wing is mounted vertically in the wind tunnel test section and subjected to an inflow velocity of  $U_\infty = 18$  m/s, corresponding to a Reynolds number of approximately  $Re_c = 120\,000$ , at various angles of attack  $\alpha$  in the range  $0^\circ < \alpha < 16^\circ$ . The measurements are performed with a FLIR SC7300 infrared camera, which is acquiring thermographic images with a resolution of  $320 \times 256$  pixels at a frame rate of 230 Hz. When heating the wing surface above the temperature of the freestream with an external heat source, such as a halogen lamp, the infrared thermography measurements of the wing surface can be used to infer the boundary layer state through the proportionality of skin friction and convective heat transfer [11]. The infrared camera measures the infrared radiation emitted from the surface of the wing, which is proportional to its surface temperature. For this study, the values of the surface temperature are of no direct interest, hence no temperature calibration is performed and the infrared thermographic data is analyzed in terms of the infrared radiation in camera counts. The experimental setup and its components in the wind tunnel are shown in Fig. 3.

## III. Workflow for the CFD Grid Generation

To obtain detailed insight into the flow physics of the Pazy Wing, a sophisticated workflow for the generation of the CFD grid was employed. Due to the built-up rib structure and the foil covering of the wing, the shape of the real wind tunnel model deviates significantly from the theoretical (CAD) model – which is designed from a NACA 0018 airfoil section and is used as the basis for manufacturing. For the real wind tunnel model, the 3D printed rib structure is covered by *Oralight*, a plastic film used for radio controlled aircraft applications. The film is applied (glued) onto the structure by heat (iron and heat gun) and shrinks once the heat source is removed. A prestressing is introduced by this approach which ensures a smooth surface even if loads are applied and the structure is deformed slightly. Nevertheless,

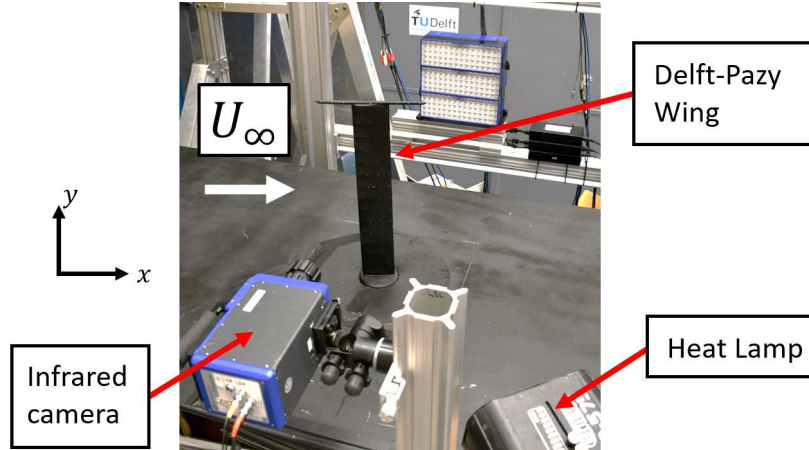


**Fig. 3 Wind tunnel setup for the infrared thermography measurements.**

an unavoidable deviation of the surface is introduced by this process because the foil sags between the ribs which leads to a modified airfoil section whose shape varies depending on the lateral position between the ribs. The outer surface of the Pazy Wing wind tunnel model from TU Delft, depicted in Fig. 4, clearly shows the sagging of the wing's foil covering. The end of the (solid) leading edge in the region between the ribs is marked by a kink (which is detailed in Fig. 4). Such details influence the flow locally and, as will be shown in the following sections, even trigger early transition. To approximate the aerodynamic simulation model as close as possible to the real wing with respect to the outer shape, the undeflected jig-shape of the Pazy Wing (without aerodynamic loading) from TU Delft was digitized using a 3D scanner. Both the cylindrical clamping section as well as the tip rod are included in the scanned surface data. The raw data of the scan were carefully processed and a highly accurate geometry model was generated by NASA which was used for the subsequent CFD grid generation. The hybrid CFD grid was built with focus on high spatial resolution of the fluid volume close to the wing in order to represent (small) geometrical details and to properly resolve the flow in the boundary layer including laminar separation bubbles as well as regions of separated flow. The surface of the wing (without the tip rod and the cylindrical clamping section) was discretized by a structured (quadrilateral) mesh with small cell sizes both in spanwise and chordwise direction to resolve the complex geometry and the associated flow features. A cut view of the CFD grid is shown in Figure 5.

In addition to the sagged wing, a CFD grid with a similar discretization was built for the clean wing configuration, i.e., without sagging of the foil covering. The geometry model was also built by NASA and as well includes the cylindrical clamping section and the tip rod. The clean configuration is used to analyze the differences to the sagged wing with respect to the flow field and transition mechanisms. Selected parameters of the grid are listed in Table 2.

**Table 2 Parameters of the unstructured hybrid CFD grid of the Pazy Wing.**

Property	Unit	Pazy Wing CFD grid
Spacing of structured quads chordwise	mm	0.3 - 0.7
Spacing of structured quads spanwise (average)	mm	1.0
first layer thickness	mm	0.0024
Number of layers	-	44
Stretching ratio	-	1.16
Total layer height	mm	10.3
Total number of elements	-	$\approx 12000000$
Total number of nodes	-	$\approx 7200000$

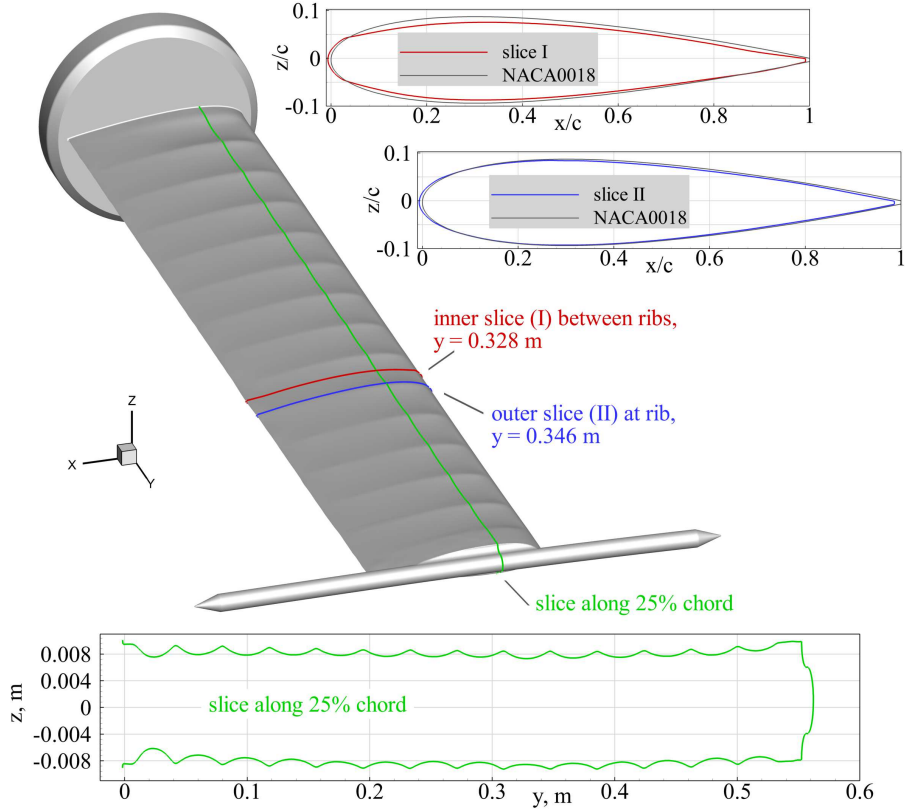


**Fig. 4** Outer surface of the TU Delft Pazy Wing (from the CFD grid) with cuts at two spanwise sections highlighting the deviations from the theoretical NACA 0018 airfoil section, which is added as reference.

## IV. Numerical Methods and Results

### A. Numerical Setup: DLR computations

The DLR TAU-Code [12] is used in this investigation. The  $\gamma$  transition model [13] is used for transition prediction in combination with the SST  $k-\omega$  turbulence model with the strain rate based definition of the eddy viscosity [14]. The  $\gamma$  transition model computes the intermittency variable  $\gamma$  in the whole flow field, thus no spanwise locations for the boundary layer stability analyses have to be prescribed as is the case for the  $e^N$  method [15]. The fully turbulent computations are performed with the SST  $k-\omega$  turbulence model. For all computations, a central scheme with artificial matrix dissipation is used for the convective flux discretization of the mean flow equations. The convective fluxes of the turbulence equations are discretized with a second-order Roe upwind scheme. A local time step is used in combination with an implicit Backward-Euler scheme to accelerate convergence employing an LU-SGS scheme for the steady computations. The dual time stepping scheme by Jameson [16] is used for the unsteady computations.

### B. Transition Behavior on a NACA0018 Airfoil at Low Reynolds Numbers

This section presents a transition model validation for a NACA0018 airfoil at low Reynolds numbers. The NACA0018 is the theoretical cross section of the Pazy Wing. The  $\gamma$  transition model is built to predict Tollmien-Schlichting transition in transonic high Reynolds number flow [13]. Although there is no lower bound for the model application in terms of Reynolds or Mach number, the  $\gamma$  transition model has not been tested extensively for Reynolds numbers below  $Re_c < 10^6$ . Especially for heavily separated flows, the prediction of laminar separation bubbles in location, size, and the related transition behavior might be insufficient. The original  $\gamma-Re_\theta$  transition model allows an increase of the intermittency up to an effective value of  $\gamma_{eff} = 2$  in separated laminar flow to limit the separation bubble size [17]. This model feature is dropped in the  $\gamma$  model as no systematic over-prediction of laminar bubble sizes is found at high Reynolds numbers, but an increase in effective intermittency might be necessary at lower Reynolds

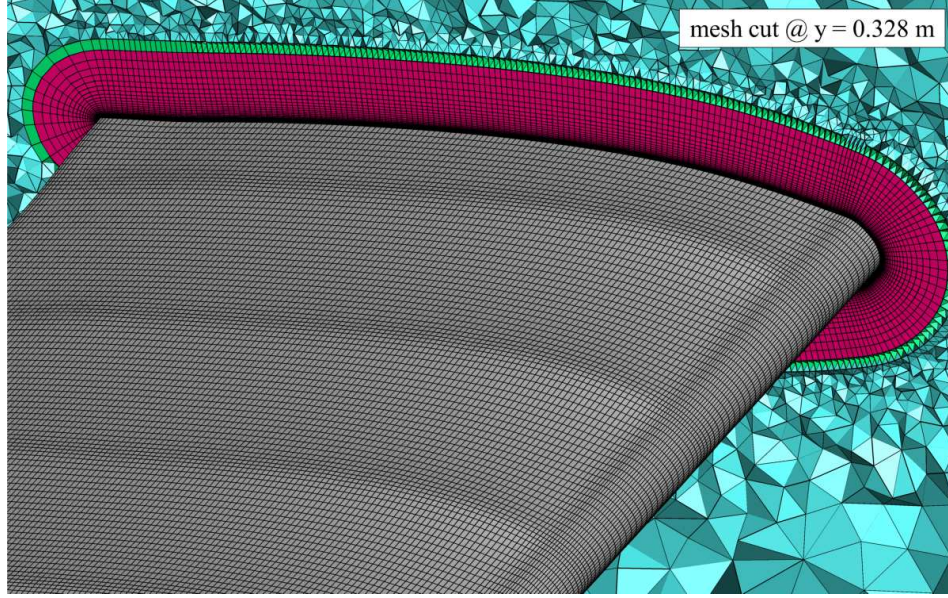


**Fig. 5** Cut view of the hybrid, unstructured Pazy Wing CFD grid with boundary layer cells. The surface is meshed by structured quadrilaterals.

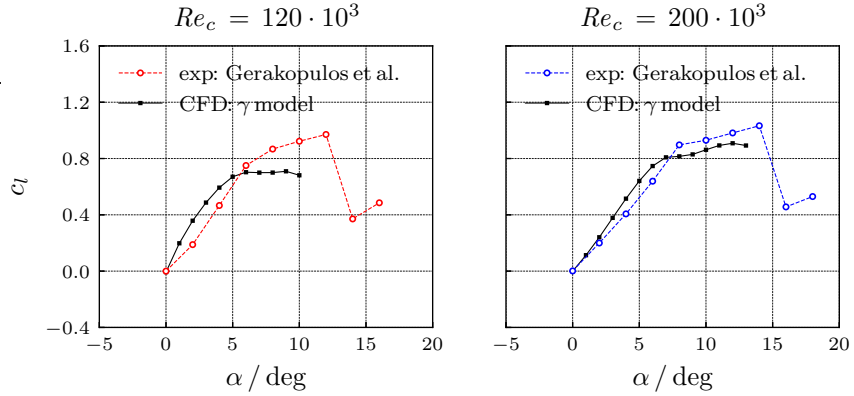
numbers. To gain more information on the transition model behavior in low Reynolds number flows, the experimental data by Gerakopoulos et al. [18] are used to further validate the  $\gamma$  transition model. Gerakopoulos et al. [18] present wind tunnel data for a NACA0018 airfoil at Reynolds numbers ranging from  $Re_c = 80 \cdot 10^3$  to  $200 \cdot 10^3$  and angles of attack of  $\alpha = 0^\circ$  to  $18^\circ$ . No specific thermodynamic conditions for the experimental setup are given, but as the wind tunnel is of an open-return suction-type, sea level conditions can be expected. According to Gerakopoulos et al. [18], the turbulence level in the wind tunnel is below  $Tu < 0.3\%$ .

Computations with the  $\gamma$  transition model for a blunt-edged airfoil of  $c = 1$  m chord length are performed at  $Re_c = 120 \cdot 10^3$  and  $200 \cdot 10^3$  for a subsonic inflow Mach number of  $M_\infty = 0.15$  at  $T_\infty = 293.15$  K and  $Tu = 0.3\%$ . The computational grid consists of 400 880 grid points. The airfoil surface is discretized with a spacing of  $\Delta x_s/c \approx 0.002$ . The  $y^+$  value of the first cell is well below 1 with maximum values of about  $y_{max}^+ \approx 0.65$  for the larger angles of attack at  $Re_c = 200 \cdot 10^3$ . The boundary layer is well covered with a structured mesh consisting of 114 layers with a wall normal growth rate of 1.1 up to a maximum wall normal spacing of  $\Delta y_s/c \approx 0.002$ . The remaining flow field is discretized using a quad-dominant unstructured grid.

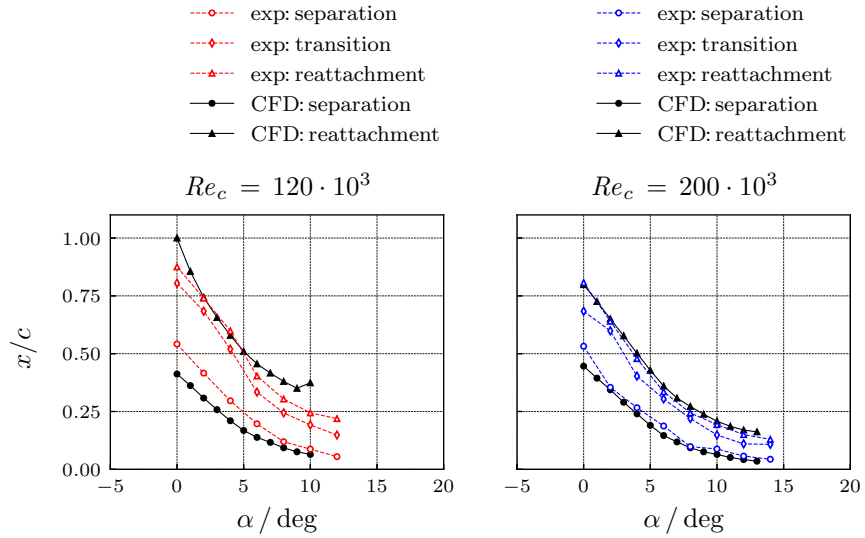
Figure 6 shows the experimental and computational lift coefficient for both Reynolds numbers. Only well converged CFD results are presented, which limits the examination to angles of attack below the lift breakdown. Especially for the lower Reynolds number of  $Re_c = 120 \cdot 10^3$ , the experiment and CFD computation agree poorly. Neither the lift coefficient, nor the lift curve slope, nor the maximum lift is predicted correctly. The agreement increases strongly with increasing Reynolds number for  $Re_c = 200 \cdot 10^3$ .

Figure 7 presents the separation behavior on the suction side of the airfoil for increasing angles of attack. The experimental separation behavior is evaluated based on the pressure coefficient distribution, for which a separation point, a transition location, and a reattachment point are identified [18]. The separation and reattachment point in the computation are directly taken as the zero crossing of the skin friction coefficient. Turbulent trailing edge separations are not included, but exist for higher angles of attack. Again, the agreement for the lower Reynolds number of  $Re_c = 120 \cdot 10^3$  is poor. The separation location is in much worse agreement than the reattachment location which indicates that the pressure gradient upstream of the separation is not computed correctly. A mismatch in the pressure distribution is most likely caused by a poor agreement in the trailing edge flow, which is determined by the upstream growth of the boundary layer and the predicted separation and transition behavior. In contrast, the results for  $Re_c = 200 \cdot 10^3$  agree very well with the experimental data.

The transition location for the  $\gamma$  transition model is not easily defined which is especially true for separated flow. It is therefore not compared to the experimental data presented by Gerakopoulos et al. [18]. The intermittency variable  $\gamma$  of the transition model is a blending function for the turbulence model. Once the transition criterion is fulfilled,



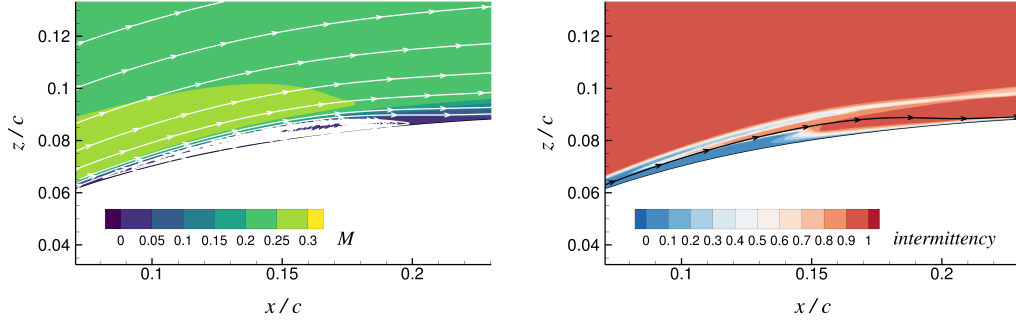
**Fig. 6** Experimental and computational lift coefficient in subsonic flow of a NACA0018 with free boundary layer transition.



**Fig. 7** Experimental and computational separation behavior at different Reynolds numbers on the suction side of a NACA0018.

the intermittency increases and production of turbulence kinetic energy starts. The transition criterion is based on experimental data but the actual model onset does not represent a meaningful location within the transition process like the indifference Reynolds number, at which disturbances start to grow, or the critical Reynolds number, at which the transition process is completed. The intermittency in the model has to increase and spread within the boundary layer to allow for any change in the boundary layer. The offset between model onset and the fully developed turbulent boundary layer state is part of the transition model calibration. The transition process itself has to be identified by secondary parameters like the skin friction coefficient distribution.

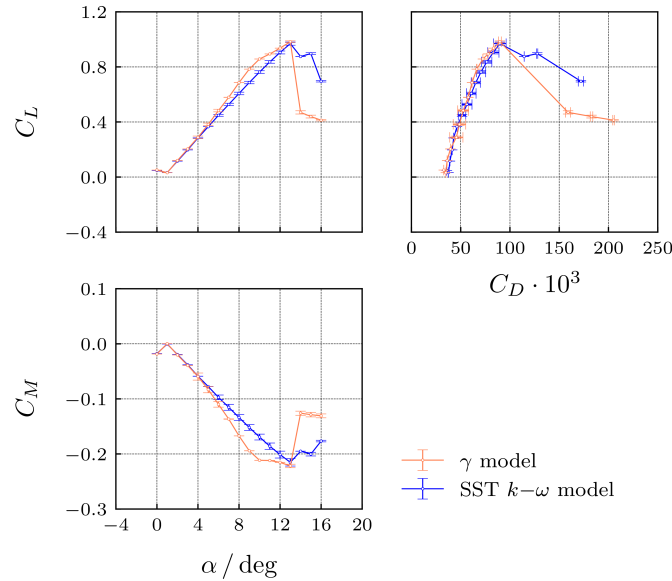
Figure 8 shows the Mach number and intermittency field at the separation bubble location on the suction side of the NACA0018 at  $\alpha = 10^\circ$ ,  $Re_c = 200 \cdot 10^3$ ,  $M = 0.15$ . The streamlines in the left part of the Figure show the recirculation area within the separation bubble (separation at  $x/c \approx 0.064$ , reattachment at  $x/c \approx 0.208$ ). The first intermittency increase is found at  $x/c \approx 0.08$  but only the strong increase of intermittency in the recirculation area enables the reattachment due to the subsequent increase in turbulence kinetic energy. A transition location might be defined based on a certain threshold of a turbulence model variable (e.g.  $R_t = \mu_t/\mu > 1$ ) but this choice might be quite arbitrary.



**Fig. 8 Mach number and intermittency field at the separation bubble location on the suction side of a NACA0018 at  $\alpha = 10^\circ$ ,  $Re_c = 200 \cdot 10^3$ ,  $M = 0.15$  with velocity streamlines.**

### C. Steady CFD Results for the Clean and Sagged Pazy Wing

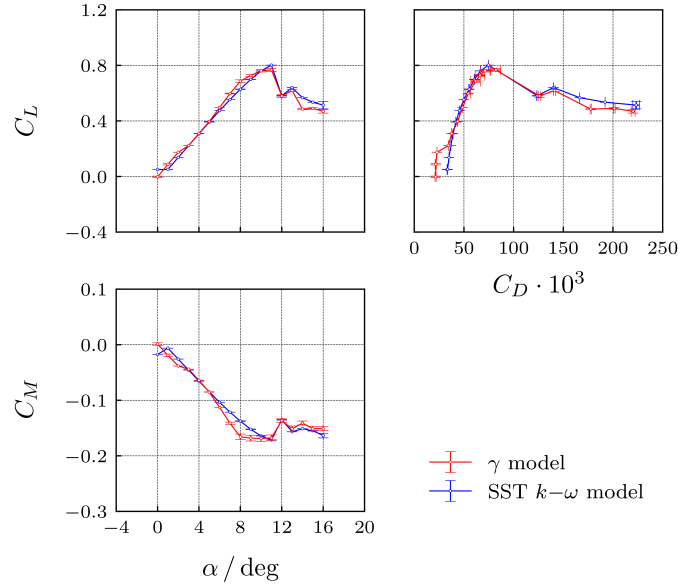
This section presents steady results for the clean and sagged Pazy Wing. The steady computations are performed at  $U_\infty = 50$  m/s at sea level conditions with  $\rho_\infty = 1.225$  kg/m<sup>3</sup>,  $T_\infty = 288.15$  K,  $p_\infty = 101325$  Pa, resulting in a Reynolds number of  $Re_c = 342165$  for  $c = 0.1$  m and a Mach number of  $M = 0.1469$ . A turbulence level of  $Tu = 0.3\%$  is kept in the computations to have a consistent numerical setup with the data presented in the previous section. Figures 9 and 10 show the fully turbulent and transitional aerodynamic coefficients for the clean and sagged Pazy Wing configuration, respectively.



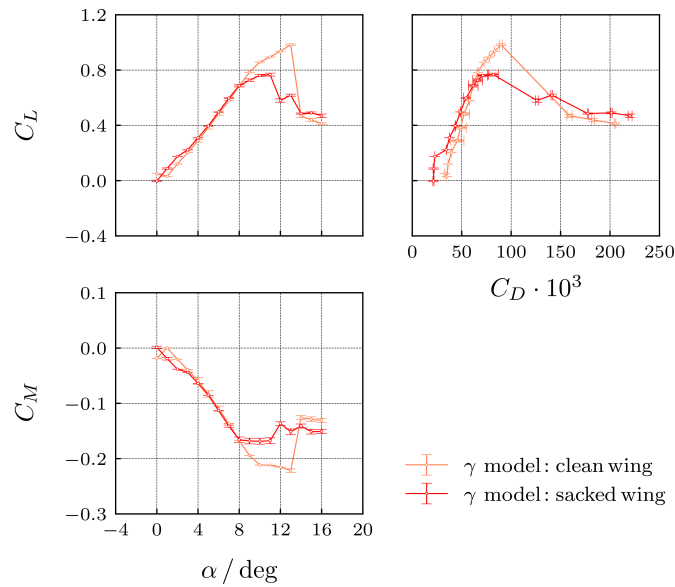
**Fig. 9 Transitional and fully turbulent aerodynamic coefficients for the clean Pazy Wing configuration.**

Figure 11 compares the transitional results for both configurations obtained with the  $\gamma$  transition model. Neither the transitional computations with the  $\gamma$  transition model, nor the fully turbulent computations with the SST  $k-\omega$  model converge to a steady result but oscillate about some mean value. This unsteady flow behavior is caused by boundary layer separations. Therefore, Figs. 9 to 11 give the mean value and the magnitude of the oscillation indicated by error bars. The transitional results do not necessarily show a worse convergence behavior compared to the fully turbulent computations.

For the clean wing configuration, the lift and moment increase for the transitional flow is only slightly larger than for the fully turbulent flow for low angles of attack. For larger angles of attack, a stronger deviation between the fully turbulent and transitional results is obtained. A similar behavior is observed for the sagged wing configuration. In



**Fig. 10 Transitional and fully turbulent aerodynamic coefficients for the sagged Pazy Wing configuration.**



**Fig. 11 Transitional aerodynamic coefficients for the clean and sagged Pazy Wing configuration.**

addition, a laminar drag bucket is found for the sagged wing around  $\alpha = 0^\circ$  with the characteristic increase in lift and moment. A laminar drag bucket usually occurs due to a decrease in the displacement thickness on the upper surface and a drag decrease due to a large amount of laminar boundary layer flow. For a case of spanwise varying heavily separated flow in combination with boundary layer transition, the effect is more obscure and will need further investigations. Figures 12 and 13 show the skin friction coefficient distribution for increasing angles of attack on the upper surface of the clean and sagged wing configuration, respectively. The black line gives the zero crossing of the skin friction value indicating separated flow regions. For the clean wing configuration in Fig. 12, a laminar separation bubble develops on the upper surface. As the angle of attack increases, the separation bubble moves upstream due to the stronger adverse pressure gradient and reduces in size. The laminar separation bubble covers the whole wing span with the exception of the wing tip area where the chordwise flow is influenced by the wing tip vortex. At about  $\alpha = 10^\circ$ , a turbulent trailing edge separation starts to develop which causes a reduced lift and moment curve slope as

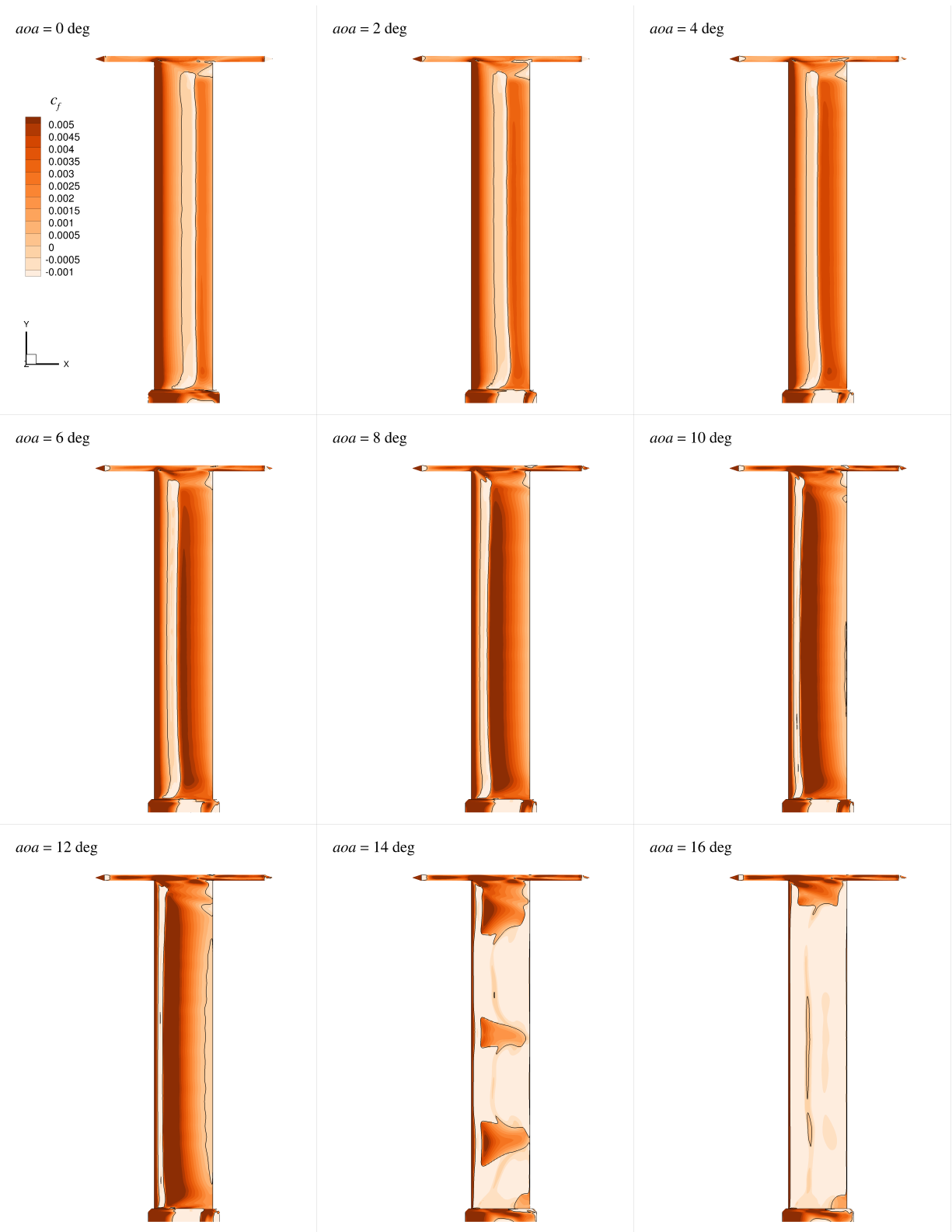


**Fig. 12** Skin friction coefficient distribution on the clean wing for increasing angles of attack for the transitional flow. The black line gives the zero crossing of the skin friction value.

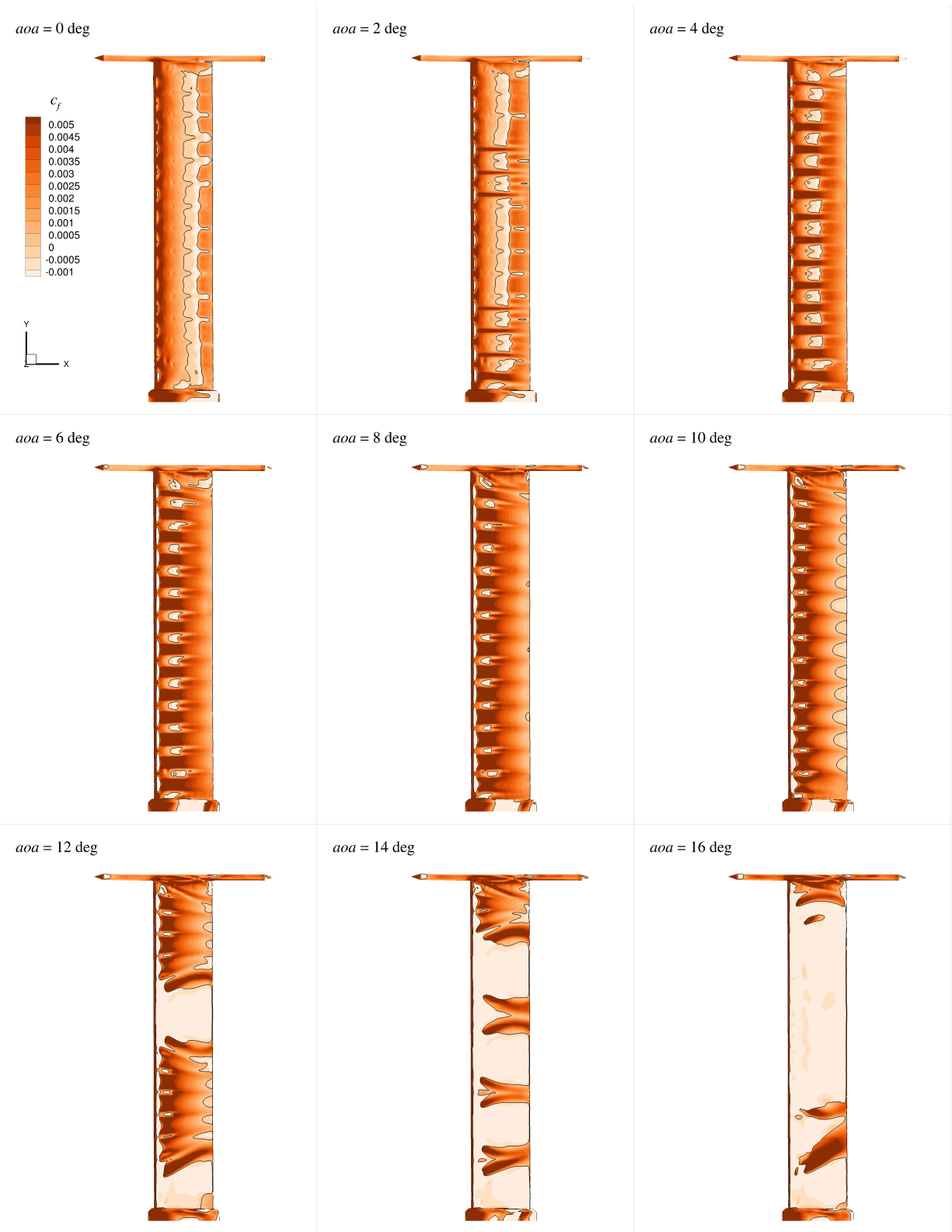


**Fig. 13** Skin friction coefficient distribution on the sagged wing for increasing angles of attack for the transitional flow. The black line gives the zero crossing of the skin friction value.

seen in Fig. 9. As the angle of attack is increased further, the flow on the upper wing surface is completely separated and the lift breakdown occurs.

The boundary layer flow on the sagged wing configuration is much more complex compared to the clean wing. At each rib location the originally intended shape of the wing is obtained. In between the rib locations, the shape is lost and the local profile is thinner and has a kink in spanwise direction. At the kink location, pockets of separated flow occur. For  $\alpha = 0^\circ$ , the boundary layer flow downstream of the separation bubble is still laminar as a spanwise flow from the ribs into the sagged regions occurs, that might stabilize the laminar flow. The intermittency only increases directly at the bubble location but vanishes further downstream. A further discussion requires more unsteady CFD computations, which are not available at the moment. Further downstream, laminar separation bubbles develop over the whole wing span. The laminar boundary layer separates further downstream at the rib locations compared to the sagged areas. As the angle of attack is increased, the boundary layer reattaches in a fully turbulent state downstream of the leading edge separations (seen by high skin friction values downstream of the separation bubble). Once the boundary layer flow becomes turbulent, the boundary layer can withstand the drag increase towards the trailing edge and a more complicated pattern of separated and attached boundary layer flow develops. As the angle of attack is increased, the leading edge separations at the kink grow in stream and spanwise size with a subsequent increase of regions with turbulent boundary layer flow downstream. At the same time, the laminar separations at the rib locations move upstream and decrease in size. As the maximum lift is approached, turbulent trailing edge separations develop in the sagged regions. A further increase in angle of attack results in a completely separated flow on the upper surface.

Figure 14 shows skin friction lines for some angles of attack on the upper surface of the sagged wing. In between

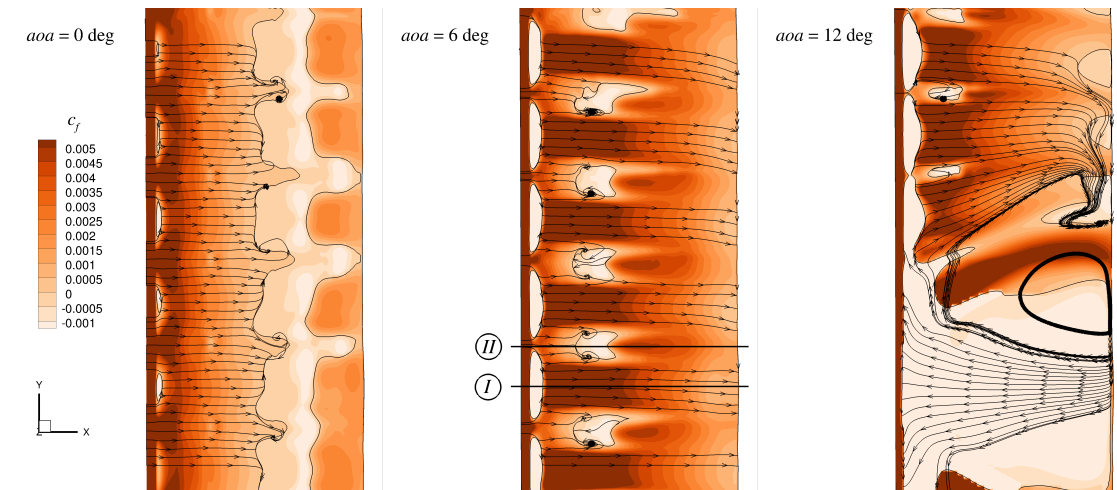


**Fig. 14** Skin friction coefficient distribution and skin friction lines on the sagged wing for increasing angles of attack in the range  $y = 0.28 \text{ m}$  to  $0.5 \text{ m}$  for the transitional flow. The black line gives the zero crossing of the skin friction value.

the leading edge separation bubbles, the entrainment effect is visible as the skin friction lines bend towards the sagged regions of the wing. For  $\alpha = 6^\circ$ , a sagged and a rib location are labeled in Fig. 14 with *Pos. I* and *Pos. II*, respectively. The geometry, pressure coefficient and skin friction distribution are shown in Fig. 15. The  $x/c$  and  $z/c$  coordinates are not scaled equally to better display the actual geometry and the kink that occurs for the sagged area at *Pos. I*. The strong pressure increase at the kink causes the laminar boundary layer to separate, undergo transition along the separation bubble and to reattach in a fully turbulent state as can be seen in the strong increase in skin friction downstream of the separation bubble. Simultaneously, the suction peak at the rib location is not strong enough to cause transition and a laminar separation bubble develops further downstream.

#### D. Experimental Validation

The numerical results for the skin friction distribution on the suction side of the wing are validated against the experimental measurements with the infrared camera in the wind tunnel. A direct quantitative comparison is not performed due to the differences in Reynolds number between the experiment ( $Re_c = 120\,000$ ) and the simulation ( $Re_c = 340\,000$ ). However, it is expected that a qualitative comparison is still suitable as a validation of the numerical

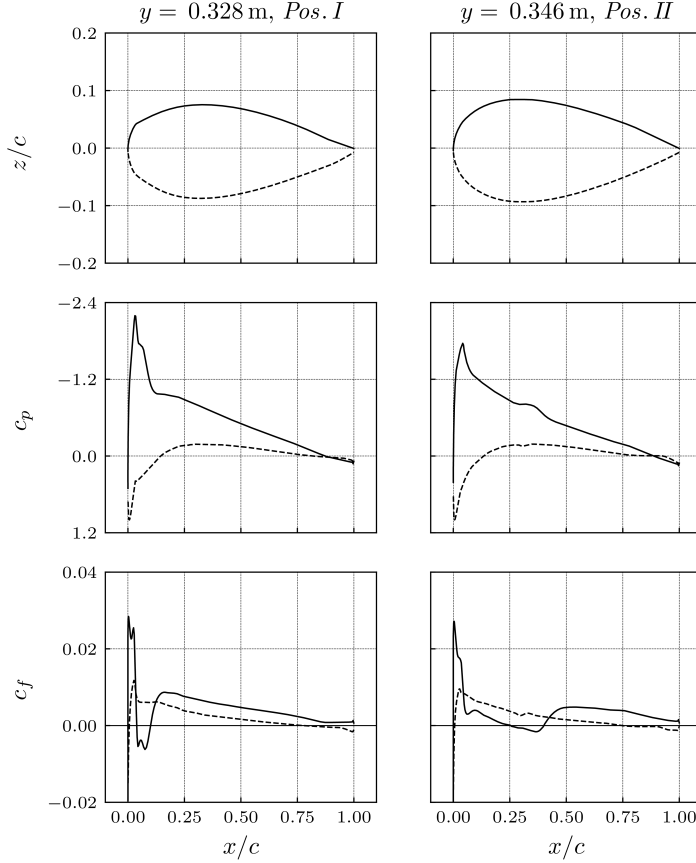


**Fig. 15** Geometry, pressure coefficient, and skin friction coefficient distribution at a sagged (*Pos. I*) and rib location (*Pos. II*) at  $\alpha = 6^\circ$  for the transitional flow. The  $x/c$  and  $z/c$  coordinates are not scaled equally to better display the actual geometry.

results because the qualitative behavior of the boundary layer does not change drastically in the considered range of Reynolds numbers, based on the results from Gerakopoulos et al. [18] shown in Fig. 7. The infrared images for increasing angles of attack from  $\alpha = 0^\circ$  to  $\alpha = 16^\circ$  are shown in Fig. 16.

The images in Fig. 16 show a section of around 250 mm of the wingspan, which is located at approximately mid-span. The displayed images are the temporal averages from a time series of 1000 acquired images for each  $\alpha$ , to diminish the effect of random measurement errors. Apart from this, no further processing is applied to the infrared image data.

The infrared thermography measurements shown in Fig. 16 are in very good agreement with the skin friction results shown in Fig. 13 over the entire range of the considered angles of attack. For  $\alpha = 0^\circ$ , a region of increased surface temperature is present, at approximately  $x/c = 0.55$  to  $x/c = 0.75$  and relatively uniform along the span, which can be linked to the region of separated flow and thus reduced convective heat transfer at this angle of attack that was observed in the CFD simulations. As the angle of attack increases, the spanwise differences of the TU Delft Pazy Wing, in terms of the cross-sectional shape on the rib locations and between them, cause significant differences in the spanwise flow pattern. The main effect that is visible in the experimental data is a reduced surface temperature downstream of the kink near the leading edge in the airfoil shape between the rib locations, suggesting that this kink causes the boundary layer to transition to turbulence and thus increasing the skin friction and with that the convective heat transfer when compared to a laminar boundary layer state. As it was observed in the CFD simulations, this effect sets in locally at individual spanwise locations at  $\alpha = 2^\circ$ , and is fully established at  $\alpha = 4^\circ$ . When further increasing  $\alpha$ , the region of turbulent flow covers a larger fraction of the span in the simulation and in the experiment, as observed in 16 through the increasing width of the darker region of lower surface temperature. For very high values of  $\alpha$ , the flow over the wing appears as fully turbulent at  $\alpha = 12^\circ$ , before at  $\alpha = 14^\circ$ , local flow separation effects cause an increased

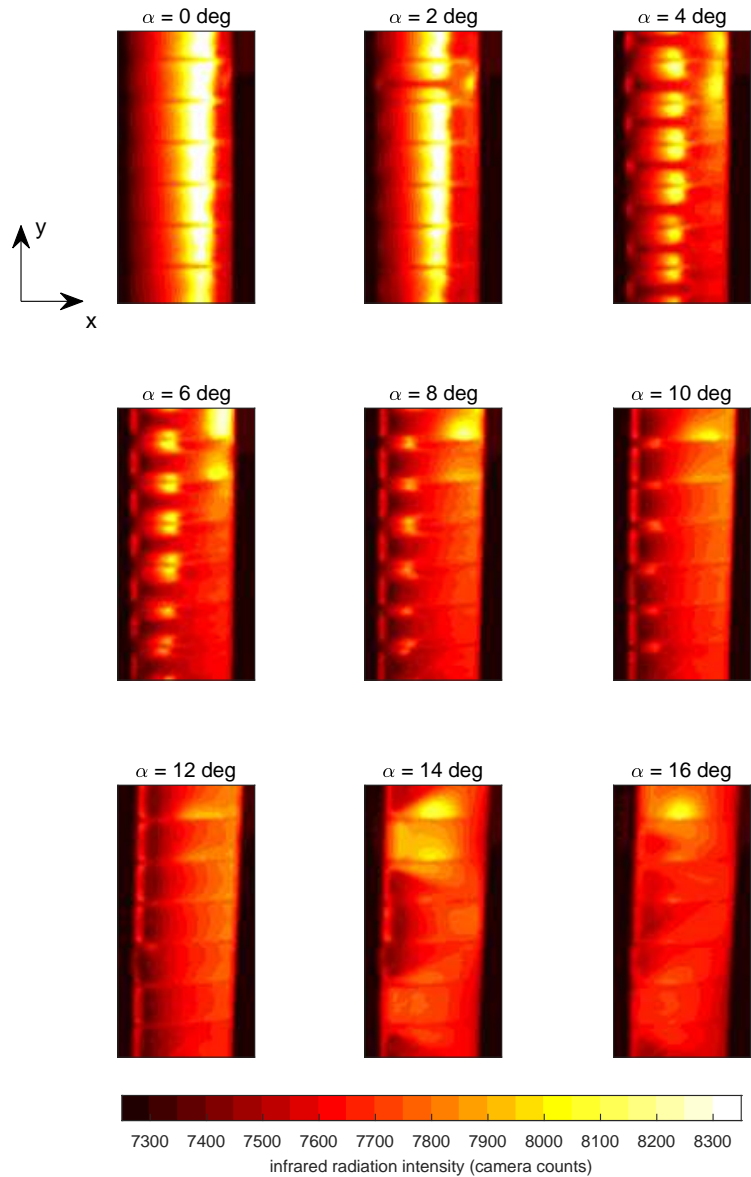


**Fig. 16 Infrared thermography images at various angles of attack.**

surface temperature at some sections of the span, before full stall is reached at  $\alpha = 16^\circ$ , indicated by a generally increased surface temperature in comparison to the turbulent attached flow. These experimental observations for very high angles of attack are in very good qualitative agreement with the CFD results shown in Fig. 13 as well.

A more detailed discussion of the experimental results and in particular of the laminar separation bubble that forms with increasing  $\alpha$  behind the kink in the airfoil shape between the ribs can be performed by inspecting the experimental temperature profiles at two different locations Pos. I and Pos. II, in between and directly on the ribs respectively, as it was done for the simulation results shown in Fig. 15. For the experimental data, this is done by first detecting the leading and trailing edge of the wing in the infrared images and then mapping the measurements on the chordwise location. The results for the temperature distributions in terms of the infrared radiation intensity for three different angles of attack at the two considered spanwise positions are shown in Fig. 17.

As visible in Fig. 17, the chordwise temperature distributions are similar between Pos. I and Pos. II for  $\alpha = 2^\circ$ , and strongly deviate between the two positions for the larger angles of attack. At  $\alpha = 2^\circ$ , the temperature increases in the chordwise direction, first slightly, which is related to the chordwise decrease in skin friction and heat transfer

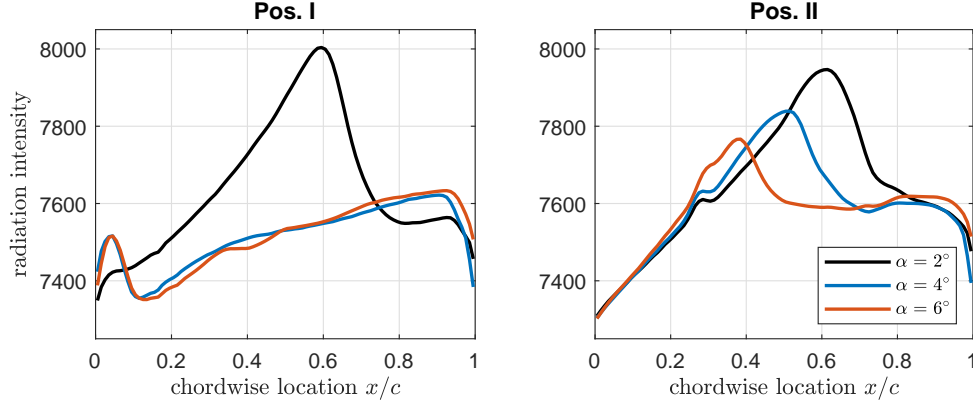


**Fig. 17** Chordwise temperature distributions between two ribs (Pos. I) and on a rib (Pos. II).

associated with the growth in laminar boundary layer thickness, and then more steeply as the flow separates and forms a laminar separation bubble. At around  $x/c = 0.7$ , the flow transitions to turbulence and subsequently reattaches, causing a steep temperature drop. A qualitatively identical behavior is observed at Pos. II for the higher angles of attack as well, where the location of the laminar separation bubble and the transition location are moving consistently upstream with increasing  $\alpha$ . Different behavior is observed at Pos. I, where a steep rise in the temperature is formed directly downstream of the leading edge as the angle of attack is increased above  $\alpha = 2^\circ$ . This can be linked to the region of separated flow that was observed in the CFD simulations to form downstream of the kink in the airfoil shape near the leading edge. Downstream of the bubble location, after around  $x/c = 0.1$  for  $\alpha = 4^\circ$  and  $\alpha = 6^\circ$ , the surface temperature is lower than at  $\alpha = 2^\circ$ , which can be explained by the higher convective heat transfer level that is associated with a turbulent boundary layer. This confirms that the kink in the airfoil in between the ribs is responsible for triggering the transition to turbulence over a laminar separation bubble, as observed in the CFD simulation results.

### E. Unsteady CFD Results for the Clean and Sagged Pazy Wing

Unsteady computations are performed to evaluate how much the time resolved flow differs from the steady solution. A time step size of  $\Delta t = 2 \cdot 10^{-4}$  sec is used, which is small enough to resolve the most important flow features. The number of inner iterations is chosen to give well converged results within each time step for the dual time stepping scheme. Figure 18 shows the time series and amplitude spectrum of the unsteady lift coefficient for the clean and sagged wing at  $\alpha = 6^\circ$ . The full and dashed red lines represent the mean value and the magnitude of the oscillations in the steady computations, respectively. The amplitude spectrum is computed for the last 0.15 sec only to exclude any transient behavior in the spectrum. The unsteady oscillations of the lift coefficient are similar for both configurations in terms of magnitude and frequency as can be seen from the amplitude spectrum of the lift coefficient. In contrast, the steady computations for the clean wing show much larger deviations from the mean compared to the steady computations for the sagged wing. A first evaluation of the unsteady data indicates that the unsteadiness of the flow is linked to the circular wind tunnel model support, but further investigations are required at this point.

Results of forced motion computations with free boundary layer transition for the clean and sagged wing are presented next. A mean angle of attack of  $\bar{\alpha} = 5^\circ$  with a pitch amplitude of  $\hat{\alpha} = 2.5^\circ$  is used to obtain similar unsteady flow conditions as given in the experimental set-up by Mertens et. al [19]. The  $\gamma$  transition model is used for transition prediction. The flow conditions are the same as for the steady computations. The mono-frequent pitch motion is computed about the  $x/c = 0.5$  chord location up to reduced frequencies of  $k = (c/2) \omega / U_\infty = 0.5$ . For each reduced frequency, 5 pitch periods are computed but only the last period is evaluated to exclude any transient behavior. Figure 19 shows the lift and moment coefficient<sup>2</sup> over angle of attack at a reduced frequency of  $k = 0.2$  and the amplitude spectrum for the last pitch period computed. The overall behavior for both wing configurations is similar. For the sagged wing, the values of the aerodynamic coefficients at the start and end of the pitch period do not match perfectly. This can indicate that there are still some transients included and more periods need to be computed but it is more likely that the base flow is unsteady itself. The steady solver run for the sagged wing at  $\alpha = 5^\circ$  does

<sup>2</sup>about the leading edge

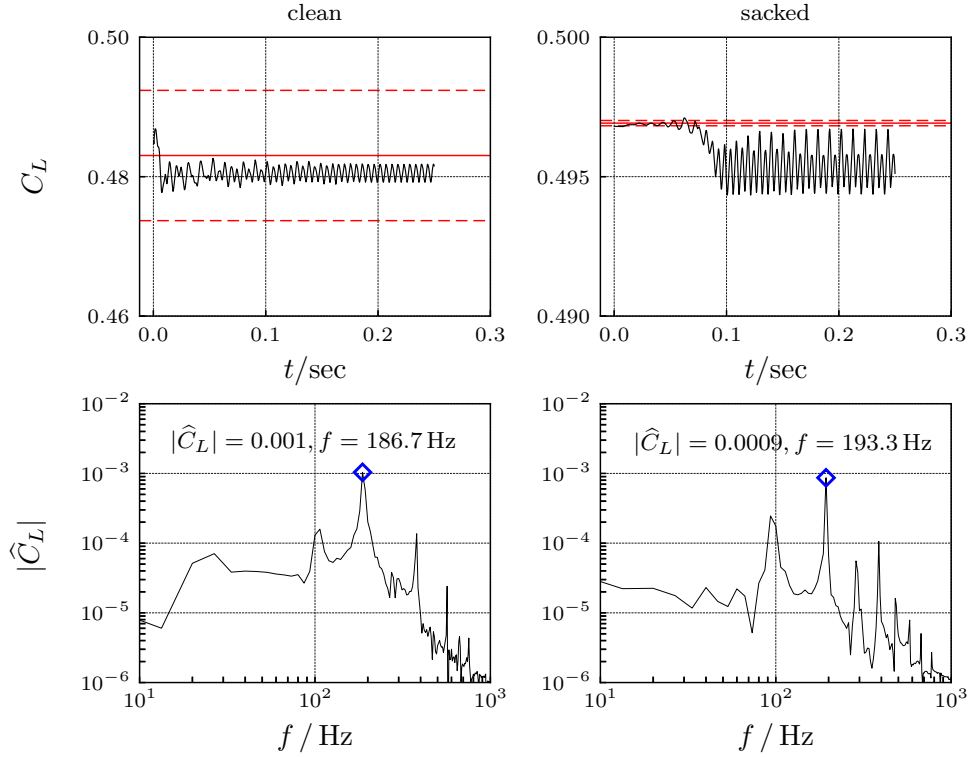


**Fig. 18** Time series and amplitude spectrum of the unsteady lift coefficient for the clean and sacked wing at  $\alpha = 6^\circ$ . The full and dashed red lines give the mean value and the magnitude of the oscillations in the steady computations, respectively.

not converge to a steady result but oscillates about some mean value which supports the latter assumption. Figure 20 shows the unsteady lift and moment coefficients with respect to pitch:  $C_{L\alpha} = \partial C_L / \partial \alpha = \text{FFT}\{C_L(t)\} / \text{FFT}\{\alpha(t)\}$  and  $C_{M\alpha} = \partial C_M / \partial \alpha = \text{FFT}\{C_M(t)\} / \text{FFT}\{\alpha(t)\}$  in magnitude and phase. The value for  $k = 0$  is determined based on the steady computations. Again, only minor differences are observed as the mean angle of attack is within the linear lift and moment curve region which is very similar for the sacked and clean configuration. In a further investigation, the unsteady transition positions need to be evaluated and compared with the experimental unsteady transition behavior presented by Mertens et al. [19].

### F. Static Coupling Methods and Results for the Sagged Pazy Wing

Results of static coupling simulations of the CFD model coupled with a nonlinear steady structural solver are presented in the following. A variety of numerical methods have been developed for the modeling of highly flexible structures. State of the art are the geometrically exact, nonlinear beam theories and the Lagrangian finite element approaches. Geometrically exact beam theories provide an elegant way to consider large deformations provided that the structure considered can be represented satisfyingly by beam elements which can pose problems in particular for complex structures and detailed models [20–23]. The Lagrangian methods use a FE mesh which is attached to the material and moves with it. Loads are applied stepwise, and the equilibrium of inner and outer loads is ensured for each load increment. The tangent stiffness matrix accounts for stresses and changes of the geometry from the last load step [24, 25]. This method is the basis of MSC Nastran’s solution sequence 400, which is used for the static coupling simulations of this work.

The structural (FE) models of the Pazy Wing test case are available, among others, in MSC Nastran format and can be used with nonlinear solution sequences of Nastran. Since the aeroelastic solver developed at DLR was used for comparable tasks in the past (coupling of potential and CFD aerodynamic methods with a commercial FE code), the beam FE model provided by the LDWG was used. This beam model was built by the University of Michigan and

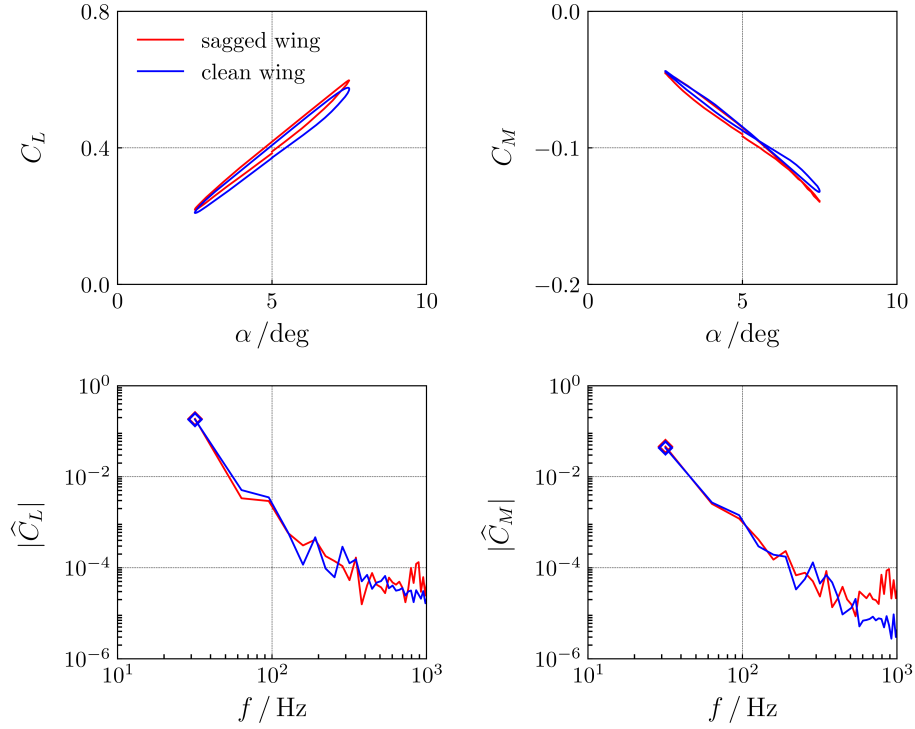


**Fig. 19** Unsteady lift and moment coefficient for the sagged and clean wing with free boundary layer transition for  $k = 0.2$  (frequency given by marker).

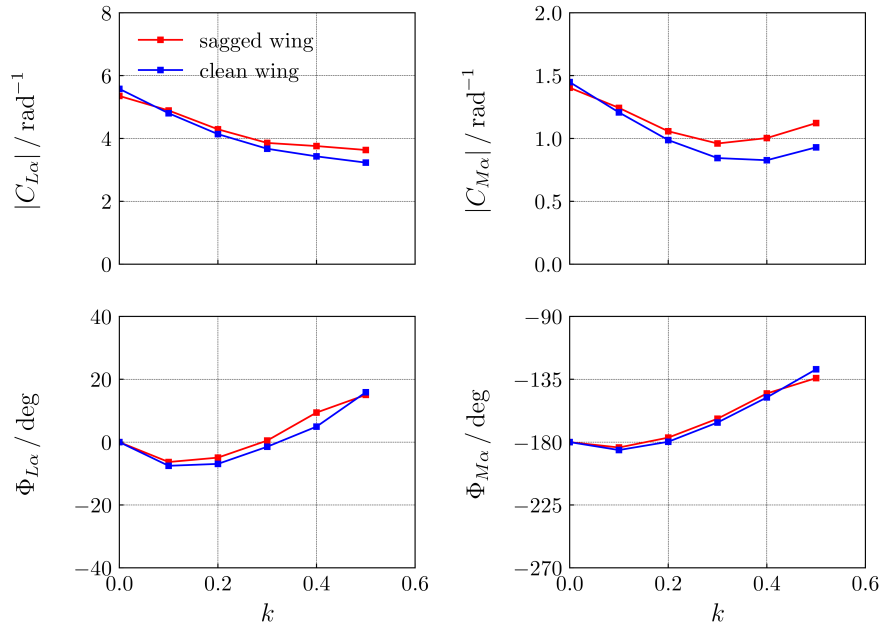


**Fig. 20** Unsteady lift and moment coefficient derivative for the sagged and clean wing with free boundary layer transition.

NASA with data from the full FE model [8, 26, 27] and enables efficient geometrically nonlinear simulations with the MSC Nastran solution sequence 400. If a beam model is to be used in coupled simulations, the aerodynamic moments must be transferred to the beam nodes. This can be done e.g. with rigid body or beam splines. Another approach is

the extension of the beam model by massless, rigid bars, which connect the outer (CFD) surface of the wing with the beam nodes. This *coupling model approach* is shown in Fig. 21 and was used with the Pazy Wing beam model.

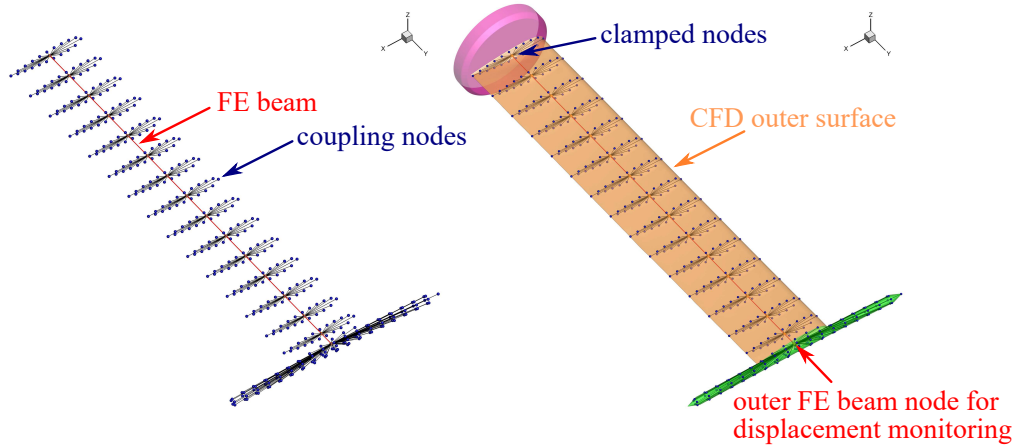


**Fig. 21** Structural and coupling model of the Pazy Wing used for the static coupling simulations. Aerodynamic forces are transferred to the coupling nodes and from there to the FE nodes of the beam via RBE2 elements.

Two methods for the modeling of turbulence and transition were applied for the static coupling simulations: The  $\gamma$ -CAS model for the modeling of free transition and the fully turbulent SST  $k-\omega$  model. In contrast to the steady and unsteady aerodynamic simulations detailed in the previous section, the  $\gamma$ -CAS transition model, which is built on the same model framework as the  $\gamma$  transition model [13, 28], but includes a modified transition onset criterion, is applied. The  $\gamma$ -CAS transition model uses the simplified Arnal-Habiballah-Delcourt (AHD) [29] transition criterion presented by Perraud et al. [30]. As the AHD criterion is based on a linear stability theory database, it is assumed that the  $\gamma$ -CAS transition model has a broader applicability and validity than the  $\gamma$  transition model, which is solely based on experimental data.

Results of the static coupling simulations are presented in Fig. 22 in terms of the displacement of the outer node of the FE model (cf. Fig. 21), which is very close to the wing tip. The airspeed is varied from 10 m/s to 60 m/s

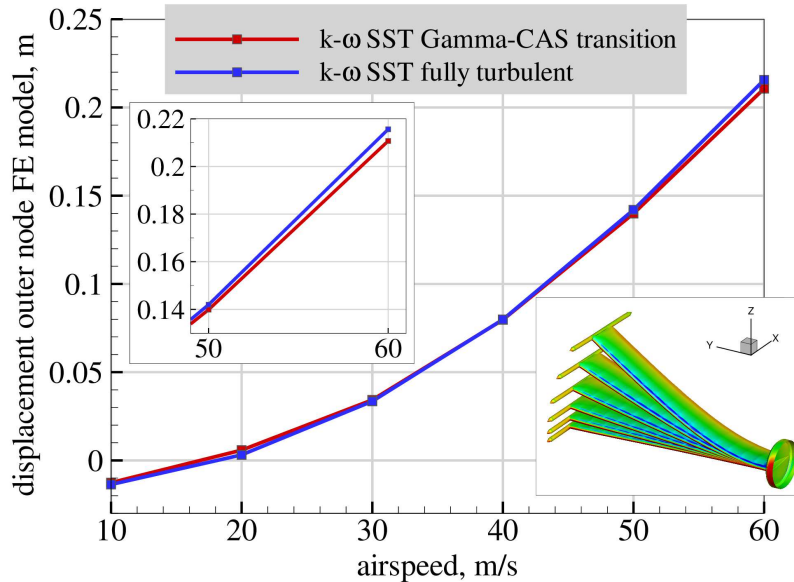


**Fig. 22** Displacement of the wing tip (outer FE beam node) of the Pazy Wing as function of airspeed calculated by static coupling CFD simulations using different methods for turbulence and transition modeling. Angle of attack is five degrees.

in steps of 10 m/s. The maximum deformation of the wing reaches remarkable values of approximately 42 % with respect to the span of the wing (which is consistent with various other static coupling and experimental results of the Pazy Wing [1, 5, 7, 9, 26, 27]). Another simulation was performed with a constant airspeed of 50 m/s and varying root angle of attack from zero to eight degrees. The displacement of the beam finite element nodes in the z direction and the rotation of the nodes about the global y axis are given in Fig. 23. The additional twist of the wing at the tip

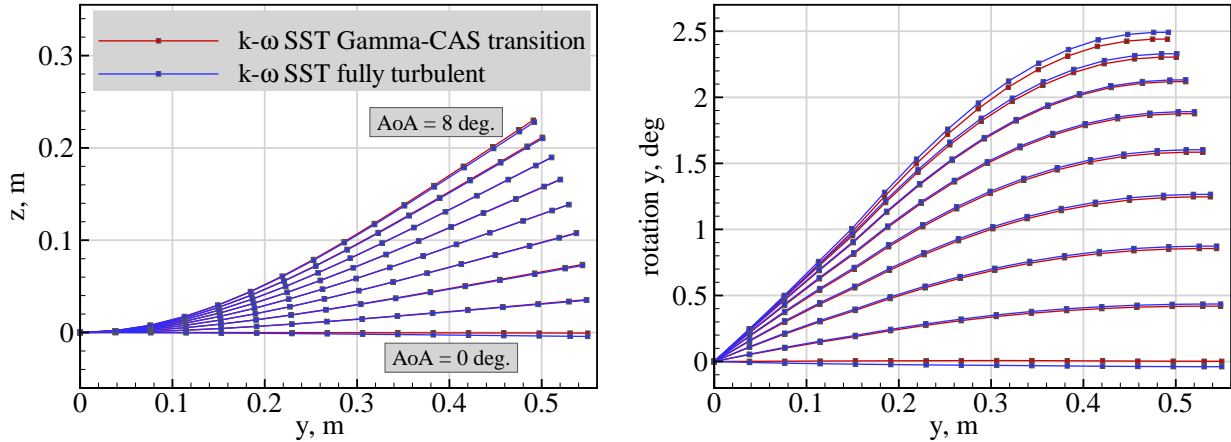


**Fig. 23 Displacement and rotation of the Pazy Wing beam nodes as function of angle of attack calculated by static coupling CFD simulations. Constant airspeed is 50 m/s.**

due to the elastic structural deformation is approximately two and a half degrees. A comparison of the skin friction coefficients for the highest angle of attack, eight degrees, is given in Fig. 24. Differences between the fully turbulent and the transitional simulation arise at the leading edge, where laminar separation bubbles are pronounced for the transitional case, and only small regions of negative skin friction coefficients emerge in the fully turbulent flow. Also the skin friction coefficient distribution close to the trailing edge is significantly different. These differences finally lead to slightly different lift coefficients and thus to slightly different structural deflections, as can be seen in Fig. 23.

As can be seen from these plots, the differences between the transitional and the fully turbulent SST  $k-\omega$  simulations are small and more pronounced for the higher airspeeds and deformations. These results seem rather sobering, i.e. the impact of the (free) transition on the structural deformations is less pronounced than could be expected when looking at the results of the steady aerodynamic simulations of the rigid wing. Higher root angles of attack could be prescribed to yield more structural deflections and thus to better analyze the impact of the free transition and fully turbulent modeling of the flow, but the maximum of approximately 42% tip deflection with respect to the span of the wing seems more realistic when compared to the experimental deflections.

However, the difference between the free transition and fully turbulent modeling approaches is expected to increase significantly when unsteady aeroelastic coupling simulations are performed. Especially at the onset of flutter and the subsequent sudden increase of oscillation amplitudes the sophisticated modeling of flow separation (including dynamic effects such as dynamic stall) is decisive. Therefore, the transitional approach should be the first to be applied for the unsteady coupling simulations in future.

## V. Conclusions

This paper presents CFD results in support of the 3<sup>rd</sup> *Aeroelastic Prediction Workshop*. The CFD data is contrasted with experimental data to validate the predicted transition behavior qualitatively. In the computations, the  $\gamma$  transition model is used. Computations for a clean wing configuration with the theoretical wing geometry and for a sagged wing geometry are performed. For the clean wing, the separation behavior is quite similar to the airfoil data. In contrast, the sagged wing shows a very complex boundary layer flow, for which spanwise varying segments of laminar and fully turbulent flow are found. Depending on the upstream boundary layer state, a very different separation behavior is observed. The data from the wind tunnel experiment show the same behavior on a qualitative level. In addition, a laminar separation bubble found at the leading edge within the sagged regions could also be verified through an inspection of the experimental temperature profiles. For most cases, no steady solution is found in the CFD

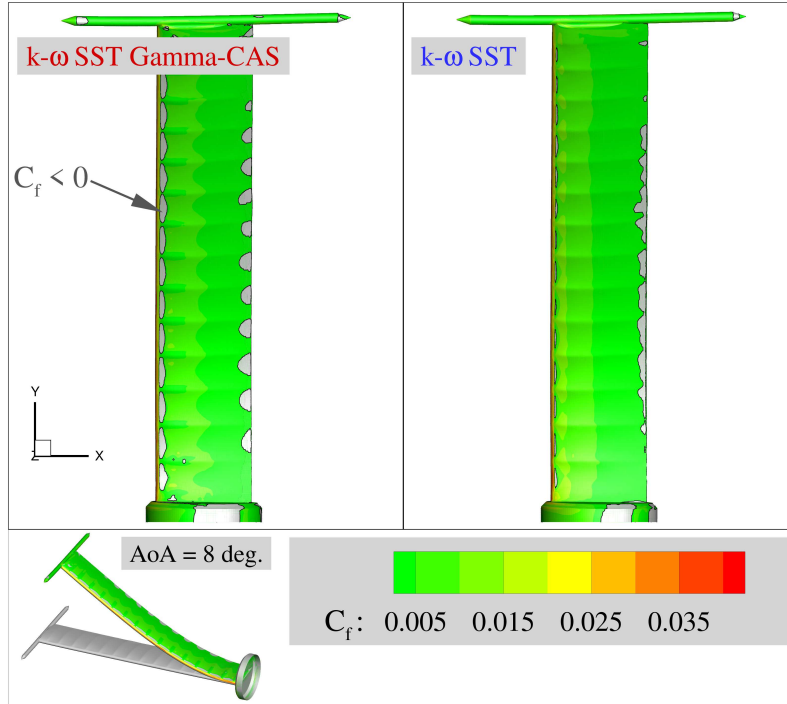


**Fig. 24** Skin friction coefficients on the upper sides of the Pazy Wing calculated by static coupling CFD simulations fully turbulent and with free transition. Reversed flow regions highlighted in light gray. Angle of attack is eight degrees, airspeed is 50 m/s.

computations and only preliminary unsteady computations could be performed for a single angle of attack. Therefore, any interpretation of flow phenomena should be done with caution as a complete set of unsteady computations for the whole lift curve would be necessary. However, the agreement between experimental and CFD data is already satisfying albeit for the higher Reynolds number in the computations. In addition, the complex flow on the Pazy Wing is fully captured by the local correlation-based transition model approach with a minimum of additional user input compared to a fully turbulent computation. Static coupling simulations in which both fully turbulent (SST  $k-\omega$  turbulence model) as well as transitional flow (SST  $k-\omega$  turbulence model in combination with the  $\gamma$ -CAS transition model) are considered yield similar results in terms of the structural deformations. Although static coupling results do not show large impact of the turbulence and transition modeling, it can be expected that unsteady aeroelastic coupling simulations yield greater differences especially with regard to limit cycle oscillations, for which flow separation are decisive mechanism.

## VI. Acknowledgments

The work of NASA to generate a highly accurate geometry file for the generation of the CFD grid based on the scanned outer surface of the TU Delft Pazy Wing is gratefully acknowledged. Furthermore, the help of the members of the Large Deflection Working Group of the AePW3 is appreciated, especially for the setup of the beam model (Cristina Riso and Bret Stanford) as well as the experimental data (Arik Drachinsky and Daniella Raveh). Also the support of the DLR Institute of Aeroelasticity for this work is acknowledged.

## References

- [1] Drachinsky, A. and Raveh, D. E., *Nonlinear Aeroelastic Analysis of Very Flexible Wings Using the Modal Rotation Method*, AIAA Scitech 2021 Forum, Virtual Conference, Jan 2021.
- [2] Ritter, M., Dillinger, J., and Meddaikar, Y. M., *Static and Dynamic Aeroelastic Validation of a Flexible Forward Swept Composite Wing*, 58<sup>th</sup> AIAA/ASCE/AHS/ASC Structures, Structural Dynamics, and Materials Conference, Grapevine, Texas, Jan 2017.

- [3] Ritter, M., Hilger, J., and Zimmer, M., *Static and Dynamic Simulations of the Pazy Wing Aeroelastic Benchmark by Nonlinear Potential Aerodynamics and detailed FE Model*, AIAA Scitech 2021 Forum, Virtual Conference, Jan 2021.
- [4] Ritter, M. and Hilger, J., *Dynamic Aeroelastic Simulations of the Pazy Wing by UVLM with Nonlinear Viscous Corrections*, AIAA Scitech 2022 Forum, Virtual Conference, Jan 2022.
- [5] Hilger, J. and Ritter, M. R., “Nonlinear Aeroelastic Simulations and Stability Analysis of the Pazy Wing Aeroelastic Benchmark,” *Aerospace*, Vol. 8, No. 10, 2021.
- [6] Drachinsky, A., Avin, O., Raveh, D. E., Ben-Shmuel, Y., and Tur, M., “Flutter Tests of the Pazy Wing,” *AIAA Journal*, Vol. 60, No. 9, Sep 2022, pp. 5414—5421.
- [7] Avin, O., Raveh, D. E., Drachinsky, A., Ben-Shmuel, Y., and Tur, M., “Experimental Aeroelastic Benchmark of a Very Flexible Wing,” *AIAA Journal*, Vol. 60, No. 3, Mar 2022, pp. 1745–1768.
- [8] Riso, C. and Cesnik, C. E., *Correlations Between UM/NAST Nonlinear Aeroelastic Simulations and the Pre-Pazy Wing Experiment*, AIAA Scitech 2021 Forum, Virtual Conference, Jan 2021.
- [9] Goizueta, N., Drachinsky, A., Wynn, A., Raveh, D. E., and Palacios, R., *Flutter predictions for very flexible wing wind tunnel test*, AIAA Scitech 2021 Forum, Virtual Conference, Jan 2021.
- [10] Righi, M., *Uncertainties Quantification in Flutter Prediction of a Wind Tunnel Model Exhibiting Large Displacements*, AIAA Scitech 2021 Forum, Virtual Conference, Jan 2021.
- [11] de Luca, L., Carlomagno, G. M., and Buresti, G., *Boundary layer diagnostics by means of an infrared scanning radiometer*, 1990, pp. 121–128.
- [12] Schwamborn, D., Gerhold, T., and Heinrich, R., *The DLR TAU-Code: Recent Applications in Research and Industry*, Proceedings European Conference on Computational Fluid Dynamics ECCOMAS, Delft, The Netherlands, 2006.
- [13] Fehrs, M., *Boundary Layer Transition in External Aerodynamics and Dynamic Aeroelastic Stability*, Dissertation, TU Braunschweig, Braunschweig, Germany, 2018.
- [14] Menter, F. R., Kuntz, M., and Langtry, R., “Ten Years of Industrial Experience with the SST Turbulence Model,” 2003.
- [15] Krumbein, A., Krimmelbein, N., and Schrauf, G., “Automatic Transition Prediction in Hybrid Flow Solver, Part I: Methodology and Sensitivities,” *Journal of Aircraft*, Vol. 46, No. 4, 2009, pp. 1176–1190.
- [16] Jameson, A., *Time dependent calculations using multigrid, with applications to unsteady flows past airfoils and wings*, 10<sup>th</sup> Computational Fluid Dynamics Conference, AIAA, Honolulu, Hawaii, 1991.
- [17] Langtry, R. B. and Menter, F. R., “Correlation-Based Transition Modeling for Unstructured Parallelized Computational Fluid Dynamics Codes,” *AIAA Journal*, Vol. 47, No. 12, 2009, pp. 2894—2906.
- [18] Gerakopoulos, R., Boutilier, M. S. H., and Yarusevych, S., *Aerodynamic Characterization of a NACA 0018 Airfoil at Low Reynolds Numbers*, 40<sup>th</sup> Fluid Dynamics Conference and Exhibit, AIAA, Chicago, Illinois, Jul 2010.
- [19] Mertens, C., Guerra, A. G., van Oudheusden, B., Fehrs, M., and Ritter, M. R., *Analysis of the Boundary Layer on a Highly Flexible Wing based on Infrared Thermography Measurements*, STAB-Symposium, Berlin, Germany, Nov 2022.
- [20] Palacios, R., Murua, J., and Cook, R., “Structural and Aerodynamic Models in Nonlinear Flight Dynamics of Very Flexible Aircraft,” *AIAA Journal*, Vol. 48, No. 11, Nov 2010, pp. 2648–2659.
- [21] Palacios, R., “Nonlinear normal modes in an intrinsic theory of anisotropic beams,” *Journal of Sound and Vibration*, Vol. 330, No. 8, Apr 2011, pp. 1772 – 1792.
- [22] Shearer, C. M. and Cesnik, C. E., “Nonlinear Flight Dynamics of Very Flexible Aircraft,” *Journal of Aircraft*, Vol. 44, No. 5, Sep 2007, pp. 1528–1545.
- [23] Jones, J. and Cesnik, C. E., *Nonlinear Aeroelastic Analysis of the X-56 Multi-Utility Aeroelastic Demonstrator*, AIAA Scitech 2016 Forum, American Institute of Aeronautics and Astronautics, Jan 2016.
- [24] Bathe, K. and Zimmermann, P., *Finite-Elemente-Methoden*, Springer, 2002.
- [25] MSC, *MSC Nastran 2017 Nonlinear User’s Guide SOL 400*, MacNeal-Schwendler Corporation, 2014.

- [26] Riso, C. and Cesnik, C. E., *Low-Order Geometrically Nonlinear Aeroelastic Modeling and Analysis of the Pazy Wing Experiment*, AIAA Scitech 2022 Forum, Virtual Conference, Jan 2022.
- [27] Stanford, B., Chwalowski, P., and Jacobson, K., *Aeroelastic Analysis of Highly Flexible Wings with Linearized Frequency Domain Aerodynamics*, AIAA Scitech 2022 Forum, Virtual Conference, Jan 2022.
- [28] François, D. G., Krumbein, A., Krimmelbein, N., and Grabe, C., *Simplified Stability-Based Transition Transport Modeling for Unstructured Computational Fluid Dynamics*, AIAA Scitech 2022 Forum, San Diego, California, Jan 2022.
- [29] Arnal, D., Habiballah, M., and Coustols, E., “Laminar Instability Theory and Transition Criteria in Two and Three-Dimensional Flow,” *La Recherche Aérospatiale*, Vol. 2, 1984, pp. 54–63.
- [30] Perraud, J., Deniau, H., and Casalis, G., *Overview of Transition Prediction Tools in the ElsA Software*, ECCOMAS 2014, Barcelona, Spain, Jul 2014.